Wood-inspired interlocking junctions using 3D-printed liquid crystal polymers

Houriet, Caroline; Ulyanov, Boris; Pascoe, John Alan; Masania, Kunal

DOI
10.1016/j.addma.2024.104590

Publication date
2025

Document Version
Final published version

Published in
Additive Manufacturing

Additive Manufacturing 97 (2025) 104590

Contents lists available at ScienceDirect

Additive Manufacturing

journal homepage: www.elsevier.com/locate/addma

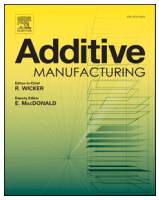

Wood-inspired interlocking junctions using 3D-printed liquid crystal polymers

Caroline Houriet [a], Boris Ulyanov [a], John-Alan Pascoe [b], Kunal Masania [a,*]

[a] Shaping Matter Lab, Faculty of Aerospace Engineering, Delft University of Technology, Kluyverweg 1, Delft 2629 HS, Netherlands
[b] Aerospace Structures and Materials, Faculty of Aerospace Engineering, Delft University of Technology, Kluyverweg 1, Delft 2629 HS, Netherlands

ARTICLE INFO

Keywords:
Wood
Junctions
Toughness
Liquid crystal polymer
Anisotropy
Waviness
Additive manufacturing

ABSTRACT

Where the trunk of a tree splits into co-dominant branches, wood fibres are highly interlocked. Such an arrangement of fibres has been shown to impart superior strength and toughness to this critical junction. Here, wavy patterns are 3D printed with a liquid crystal polymer (LCP) to evaluate the potential of wood-inspired localized adaptations to improve the robustness of junctions between orthotropic struts. The highly anisotropic, fibrillar microstructure of LCPs is harnessed by Fused Filament Fabrication, yielding Young's modulus and tensile strength reaching 30 GPa and 500 MPa respectively. However, unidirectional 3D-prints subjected to normal tensile stresses show weak interfaces, like in wood. To overcome this weakness, sinusoidal, helix and sawtooth patterns are 3D-printed to create interlocking between layers. A trade-off is established between uniaxial tension and short-beam shear with increasing interlocking angle of the sinusoidal pattern. We find that the work associated with crack propagation in Mode I is increased three-fold compared to a unidirectional pattern, through extrinsic toughening. When applied to a more complex load case in a curved beam in four-point bending, helix-patterning at the junction zone increases the maximum load by 88 %. By locally controlling anisotropy via waviness, this method opens the possibility of improving toughness and transverse properties where the stress state is multi-axial without adding mass in future recyclable structural materials.

1. Introduction

The mechanical anisotropy displayed by biological materials such as wood grants them multi-functionality and adaptability while often making optimal use of scarce resources[1]. Anisotropic materials can also be produced by additive manufacturing, allowing the simultaneous control of topology and orientation. Finding concurrently the optimal topology and directionality for a given load case has also been the purpose of numerical approaches[2–4]. These Topology and Anisotropy Optimisation (TAO) schemes typically output "organic-looking" geometries where struts are smoothly connected at multiple angles to form junctions. Struts tend to be loaded either in compression or tension, similar to conventional truss structures[5]. Junctions, however, are subjected to more complex loads. While for truss configurations, junctions can be treated like pin-joints as the moments transmitted through them are negligible, current topology optimisation schemes do not offer this guarantee. In these designs, as loads are transferred from one strut to its neighbours, the junctions see a combination of tensile, shear and compressive stresses in multiple directions[6]. Optimizing fibre placement accordingly is therefore crucial to the strength of TAO objects, and ultimately to their applicability in demanding scenarios. Several computational works have also introduced the anisotropy level itself as a design variable, along with density and directionality[2,4,5,7]. For instance, in Schmidt et al[2]. , the algorithm is set to optimize topology and simultaneously choose a material configuration between the bounds E1:E2 = 50:10 (orthotropic) and E1:E2 = 18:18 (isotropic). The resulting geometry uses orthotropy everywhere except at junctions, where isotropy is deemed more efficient. The work of Kundu et al[5]. has also included the tensile/compressive asymmetry of the failure envelope, highlighting the potential of such a design variable for strength considerations. This illustrates the need for a manufacturing approach where anisotropy levels can be tuned and especially led towards more isotropy at junctions.

To manufacture a part with orthotropic struts and a seamless transition towards isotropic junctions, on-the-fly gradients of material properties are needed. Material properties can be changed with infill type and direction[8], but challenges remain in obtaining continuity between the printed lines and smooth transitions between different

* Corresponding author.
E-mail address: k.masania@tudelft.nl (K. Masania).

https://doi.org/10.1016/j.addma.2024.104590
Received 3 July 2024; Received in revised form 27 October 2024; Accepted 3 December 2024
Available online 5 December 2024

anisotropic and isotropic zones. Spinodoids[9,10] and variable unit cells [11] can be used to obtain smooth anisotropy gradients with a single isotropic printing material. Other manufacturing methods focus on stirring short-fibre composite via rotational shear[12], or the physical mixing of two materials[13–15].

The scarcity and implementation difficulties of mechanical gradients with synthetic materials are in stark contrast to their prevalence in biological materials[16]. Trees are primary examples of anisotropic structures with complex geometries with multiple junctions. Co-dominant tree forks, in particular, have to sustain two important goals: continued nutrient transport between roots and leaves, and maintain structural integrity[17]. As pointed out by Slater et al. [18], the resulting directionality of these junctions shown in Fig. 1**a** differs from the simpler 'Engineered' configuration of Fig. 1**b**. The main difference takes place at the central apex of the fork (the tip of the 'Y') where axillary wood can be found. This important biomechanical attribute of junctions in trees is a type of reaction wood characterized by its tortuous interlocked grain[19], as shown in Fig. 1**a.** Triggered by thigmo-morphogenesis (mechanical stimulus)[20], it tends to form under the junction bark ridge and is the most developed when the two branches measure approximately the same diameter[17,19,21]. The central apex of co-dominant forks has been measured to be five times tougher than side regions, due to both its higher density and the interlocking pattern[22]. Impressively, this reinforced zone was reported to show fracture resistance within the interlaminar plane 1.5 times larger than normal to it. While interlocking is a large contributor to the reinforcement of the apex region, multi-scale toughening mechanisms are numerous on the branch-stem interface of trees. Among others, they include crack-bridging by aggregates of microfibrils, crack tip blunting, and zig-zag crack deflection at cell wall interfaces[23,24].

Because of the difficulty and time necessary to shape living wood [25,26], digital fabrication has been instrumental in integrating desirable wood features into other materials. Sinusoidal-like or tortuous patterns have been also widely studied and reproduced to create interlocking interfaces with 3D-printing[27–30] or composite technologies [31–33], with some studies aiming to reinforce T-joints[34,35]. 3D-printing wood-like features has also been attempted with helical cylinders to reproduce micro-fibril angles[36,37]. However, there remains a gap in knowledge in harnessing anisotropy to realise tuneable gradients of mechanical properties at junctions.

Here, wavy and helical features, inspired by the characteristic tortuosity of axillary wood, are 3D-printed and studied using liquid crystal polymers (LCPs). Their main advantage is strong anisotropy with unlimited shaping freedom due to the absence of discrete physical reinforcement such as fibres[38,39]. Liquid crystallinity is characterized by the presence of local directional order of the molecules in the liquid state at the scale of nematic domains of a few micrometres in size[40]. As the rigid rod-like polymer chains pass through the contracting die of the nozzle, elongational and shear flow align the nematic domain in the same direction[41]. As the 3D-printer nozzle translates, it deposits the molten material which aligns with the extrusion direction, as illustrated in Fig. 1**c.** When exposed to ambient temperatures, the material cools down before the relaxation of the directors can take place, resulting in the preservation of this alignment in the solid state[39]. Three routes to tune the anisotropy of this material have been explored: via annealing and changing printing temperature [39,42], embedding spun fibres as

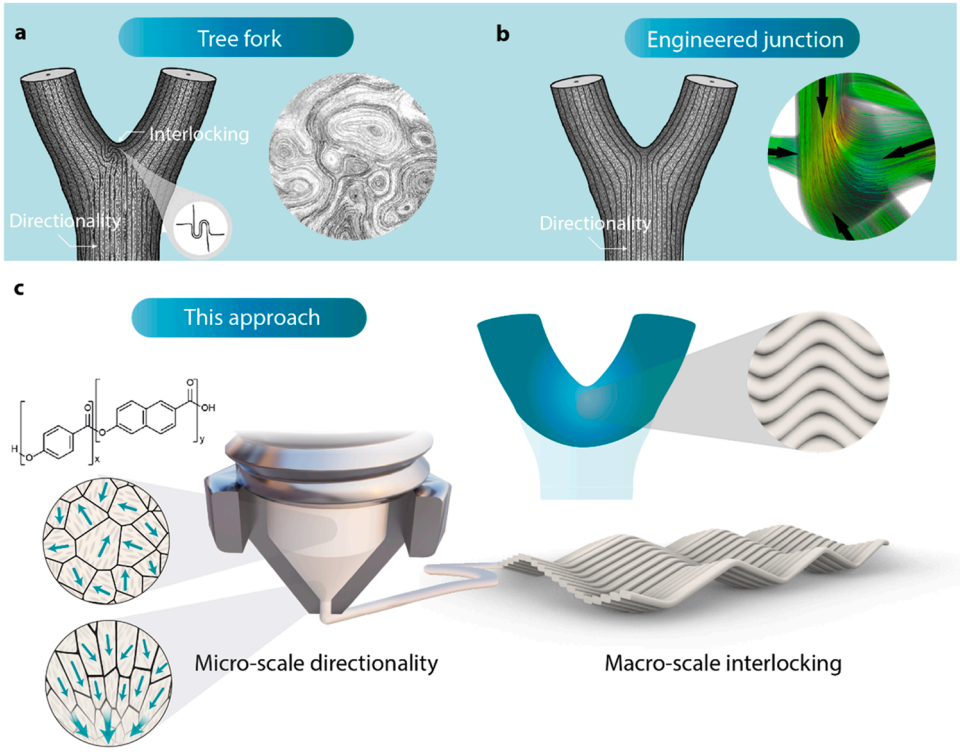

Fig. 1. Zones created where multiple mechanical struts are brought together are called junctions. They are found in most topology-optimized geometries, and in natural materials, such as tree branches and forks. For anisotropic materials, the transition from an orthotropic strut with a given orientation to another one can be achieved via multiple routes. **A.** In the "contour-like" engineering route, the simplicity of the toolpath and continuity of the fibres are prioritized, associated with the shortest path between two struts. **B.** Similar natural structures such as main forks in trees also need to conduct nutrients from root to foliage[19]. At the apex of their junction, denser axillary wood shows a tortuous, interlocking grain. **C.** Approaching isotropy at junctions with an anisotropic material, while keeping continuous toolpaths, is therefore possible for wood by using interlocked patterns. To replicate these biological patterns, liquid crystal polymers (LCP) can be readily extruded with Fused Filament Fabrication, allowing the aligned domains to be deposited in the direction of travel. Straight lines can turn into sinusoidal paths with nozzle motion to provide tortuosity at desired locations.
(a) Reproduced from [18] with permission from Talor & Francis. (b) Reproduced from [19] and [2] with permission from Springer.

reinforcement to the 3D-printed part[43], or changing the line width [38]. Through the latter approach, mechanical gradients can be achieved within the same toolpath between 3 and 30 GPa of Young's modulus. Furthermore, the absence of manufacturing constraints like curvature opens the possibility of creating anisotropic patterns seldom seen in engineering materials, such as spirals.

Due to the fibrillar nature of this material, its interlaminar adhesion highly depends on processing conditions and is a point of caution [42, 44]. We hypothesize that the interlocking created by waviness will promote a shear behaviour that dissipates energy through the delamination of fibrils. To explore the potential of such patterns, their properties in tension, short-beam shear, as well as toughness are measured for different planes, with varying wavelengths and amplitudes. Comparing the behaviour in four-point bending of unidirectional contour-like patterns to wavy patterns at the junction zone between two struts reveals an 88 %-increase in load with this strategy. By tuning anisotropy and creating interlocking while keeping the toolpath continuous, this research opens new avenues for the manufacturing of TAO parts with complex, robust junctions adapted to complex load cases.

2. Materials and methods

2.1. Toolpath generation

Custom toolpaths are created using Rhino 7 (MacNeel, USA) with the

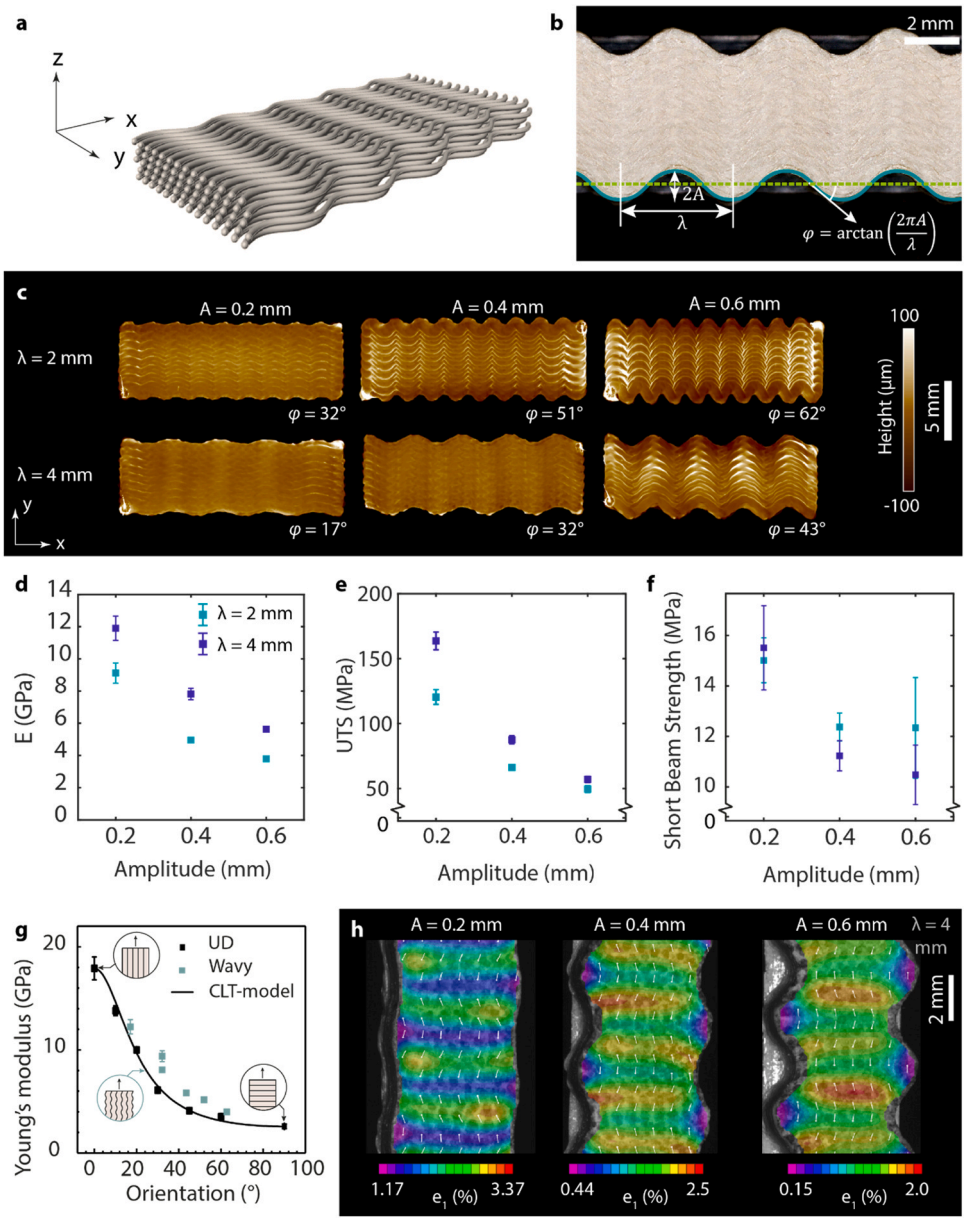

Fig. 2. Liquid crystal polymers 3D-printed with different waviness parameters. **A.** The sinusoidal path lies within the build-plane, normal to the Z-direction. **B.** Increasing amplitude A or decreasing wavelength λ results in an increase of φ, the angle between the longitudinal axis X and the steepest slope of the sine. **C.** Height map of the top surface of short-beam shear samples. **D.** Young's modulus and **E.** Ultimate Tensile Strength (UTS) decrease with increasing amplitude and decreasing wavelength. **F.** Increasing amplitude also reduces short-beam shear strength. **G.** Young's modulus of the wavy samples is plotted against their maximum angle deviation φ, following the trend obtained from unidirectional parts with different printing angles in Gantenbein et al[39]. The stiffness of the wavy samples corresponds to their unidirectional counterparts oriented at an angle φ. **H.** Digital Image Correlation of typical tensile samples before failure reveals that the strain distribution is highly heterogeneous, with deformations at their maximum at φ. Colours and arrow orientation represent respectively the amplitude and direction of the principal strain ϵ_1.

visual programming platform Grasshopper.

2.2. 3D-printing

The thermotropic random copolyester HBA: HNA (4-hydroxybenzoic acid and 6-hydroxynaphtalene-2-carboxylic acid) with ratio 73:27, is supplied as filament by NematX AG (Switzerland). The filament is printed on a Prusa MK3S+ 3D-printer, modified to withstand slightly larger temperatures than its specification. Printing temperature is 295°C except in Fig. 5 where 330°C is chosen to facilitate manufacturing of the standing compact-tension specimen in an enclosure. Layer height is fixed to 0.05 mm for Figs. 2 and 3, and to 0.1 mm for Figs. 4, 5, 6. Print speed is set to 35 mm/s and linewidth is 0.35 mm for a nozzle (E3D V6) diameter of 0.4 mm.

2.3. Microscopy

A VR-5000 wide-area 3D microscope (Keyence, Japan) was used to measure the surface profile of representative samples for each pattern and calculate the arithmetic average surface roughness (Sa) of fractured surfaces of compact-tension specimens, with $Sa = \frac{1}{A}\iint_A |Z(x,y)|dxdy$. A correction is applied by removing the roughness value of a perfectly smooth bi-sinusoidal shape, to only consider local, "textural" roughness.

2.4. Mechanical testing

2.4.1. Tension

Unidirectional samples of 110x5x2 mm are 3D-printed and tested with a 10 kN universal testing machine (Zwick-Roell, Germany) with a 10 kN load cell, at a rate of 2 mm.min^{-1} following ISO 527–5. The specimens are bonded to glass-fibre end tabs with DP160 adhesive (3 M, USA) for consistent load introduction. A hydraulic grip system is used to prevent slippage of the specimen. A minimum of five specimens are tested per batch. Ultimate Tensile Strength is calculated by P_{max}/A where P_{max} is the maximum load recorded, and A the specimen cross-section at the gauge length. The Young's modulus is calculated by the slope of the linear fit of the stress-strain curve in between DIC-measured strain values of 0.1 % and 0.3 %.

2.4.2. Short-beam shear

Samples of dimensions 18x6x3 mm are tested in three-point bending. The span length is adjusted according to the standard ASTM D2344 to four times the specimen thickness with a tolerance of 0.3 mm. The load is introduced by a three-point bending fixture with side supports diameters of 3 mm, and a centered load introduction head of 6 mm in diameter. Deformation is measured by the displacement of the central pin with respect to its initial position after a pre-load of 5 N. The test is performed on a 10 kN universal testing machine (Zwick-Roell, Germany) with a 1 kN load cell at a speed of 1 mm.min^{-1}. Short-beam shear strength is calculated by the formula $\sigma_{SBS} = 0.75\, F_{max}/(bh)$ where b and h are the width and thickness of the specimen, respectively, and F_{max} is the maximum load recorded. Five to seven specimens are tested per batch.

2.4.3. Mode-I fracture with compact tension

Samples of dimensions 35 × 33.6 × 7 mm are 3D-printed following ASTM standard D5045, with the holes for the loading pins and the notch integrated in the geometry. The notch is further sharpened by razor drawing with gentle pressure to create a starter dent. A 10 kN universal testing machine (Zwick-Roell, Germany) is used with a 1 kN load cell and a strain rate of 10 mm.min^{-1}. A minimum of five specimens are tested per batch. Load-displacement values are recorded until complete dissociation of the specimen, but data is considered until the slope reaches a value of 0.02 consistently for 100 data points.

2.4.4. Four-point bending

Curved-beam specimens are tested in four-point bending with a top span length of 60 mm and a bottom span length of 50 mm, with a diameter of 10 mm for the support rods and loading rods. Since the geometry is beam-like with a 10 × 8 mm cross-section that may show instability in the out-of-plane direction during loading, strong cylindrical magnets are placed on the support rods to secure the specimen in a vertical position during load introduction.

2.4.5. DIC

Digital Image Correlation is used to measure the deformation of tensile specimens. Two 9 MP cameras (LIMESS, Germany) with a 50 mm-focal length lens were used to acquire images at a rate of 2 Hz. The analysis is performed using Vic-3D 8 (Correlated Solutions), with a subset size and step size of 27 and 7. This enables the use of a digital

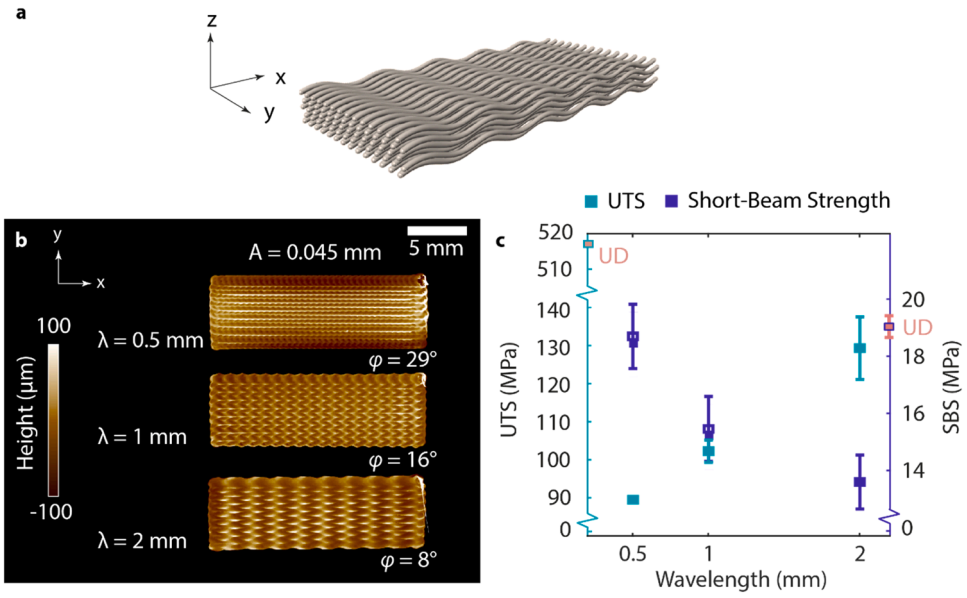

Fig. 3. A. Sinusoidal toolpath located within the XZ plane. **B.** Height map of short-beam shear samples with varying wavelengths showing the waviness pattern. **C.** Samples with different wavelengths show a clear trade-off can be made between ultimate tensile strength and short-beam shear strength.

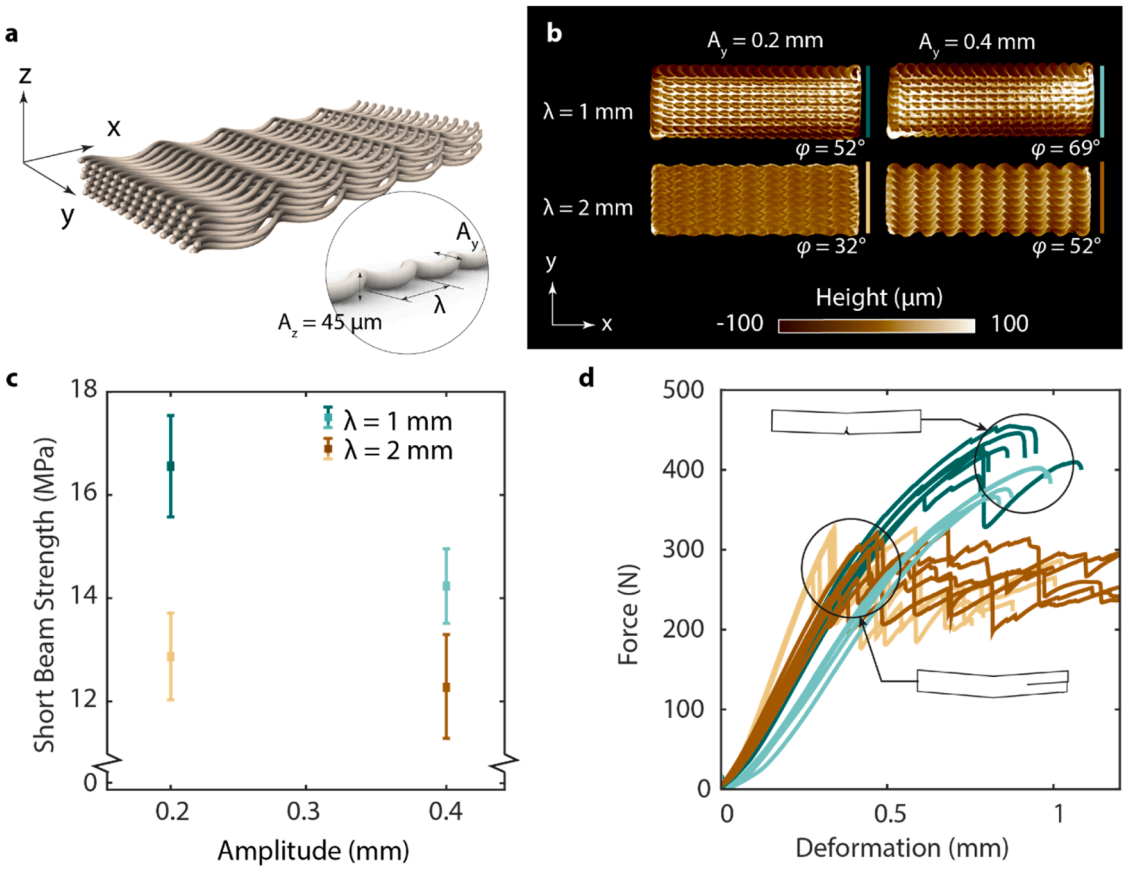

Fig. 4. Helicoidal toolpath, with waviness in the XZ and XY plane. **A.** The helix is ellipsoidal, as different amplitudes are used for the sinusoidal shapes in both planes, with $A_y > A_z$. **B.** Height maps of samples with corresponding parameters (A_y, λ). **C.** The average SBS value is shown against A_y, indicating that smaller pattern sizes are still beneficial for SBS with helical patterns. Error bars correspond to standard deviations. **D.** Force-displacement curves show two kinds of fracture mode: for the lower performing samples with $\lambda =$ 2 mm, fracture takes place in interlaminar shear, while for the highest ones, tensile fracture takes place, indicating a superior interlocking effect.

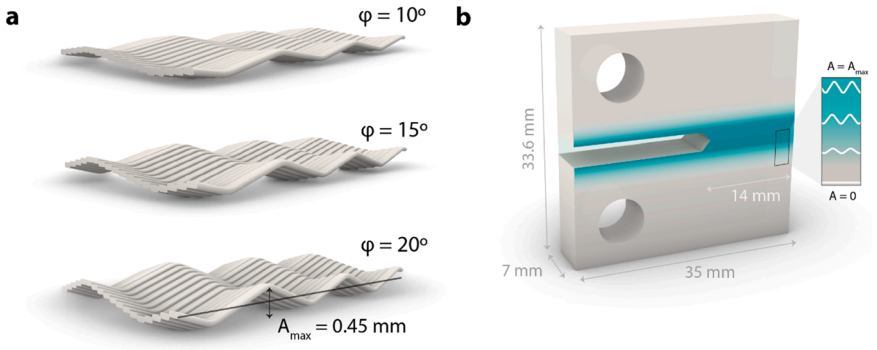

Fig. 5. Bi-sinusoidal pattern applied to Compact Tension specimens. **A.** Three surfaces are tested, for which $\lambda = 5$ mm and φ makes an angle of 10, 15 and 20° to the X-axis. **B.** The Compact Tension specimen geometry is printed standing, with a gradual amplitude increase to reach a fully developed pattern throughout the height of the notched region.

extensometer to obtain strain values for Young's modulus calculations.

3. Results and discussion

3.1. Waviness parallel to build plane

To study whether waviness can be used to vary tensile properties and shear properties of 3D-printed LCP, samples with variation along the XY direction, i.e. perpendicular to the build deposition direction, are manufactured as shown in Fig. 2. The parameters studied for these planar infills are shown in Fig. 2**a and b.** The infill line is described by the curve $A\sin(\frac{2\pi}{\lambda}x)$ where A is the amplitude and λ is the wavelength. The maximum angular deviationto the longitudinal direction is $\varphi = \arctan\frac{2\pi A}{\lambda}$. It spans from sample (A = 0.2, λ = 4 mm) with $\varphi = 17°$ to sample (A = 0.6, λ = 2 mm) with $\varphi = 62°$. For a comparison of surface quality between the six types chosen with varying wavelength and amplitude, the resulting top surface of 3D-printed samples is coloured according to the deviation to its average height within ± 100 µm in Fig. 2**c**. Their Young's modulus and Ultimate Tensile Strength (UTS) are plotted against amplitude in Figs. 2**d and** 2**e**, respectively. The general

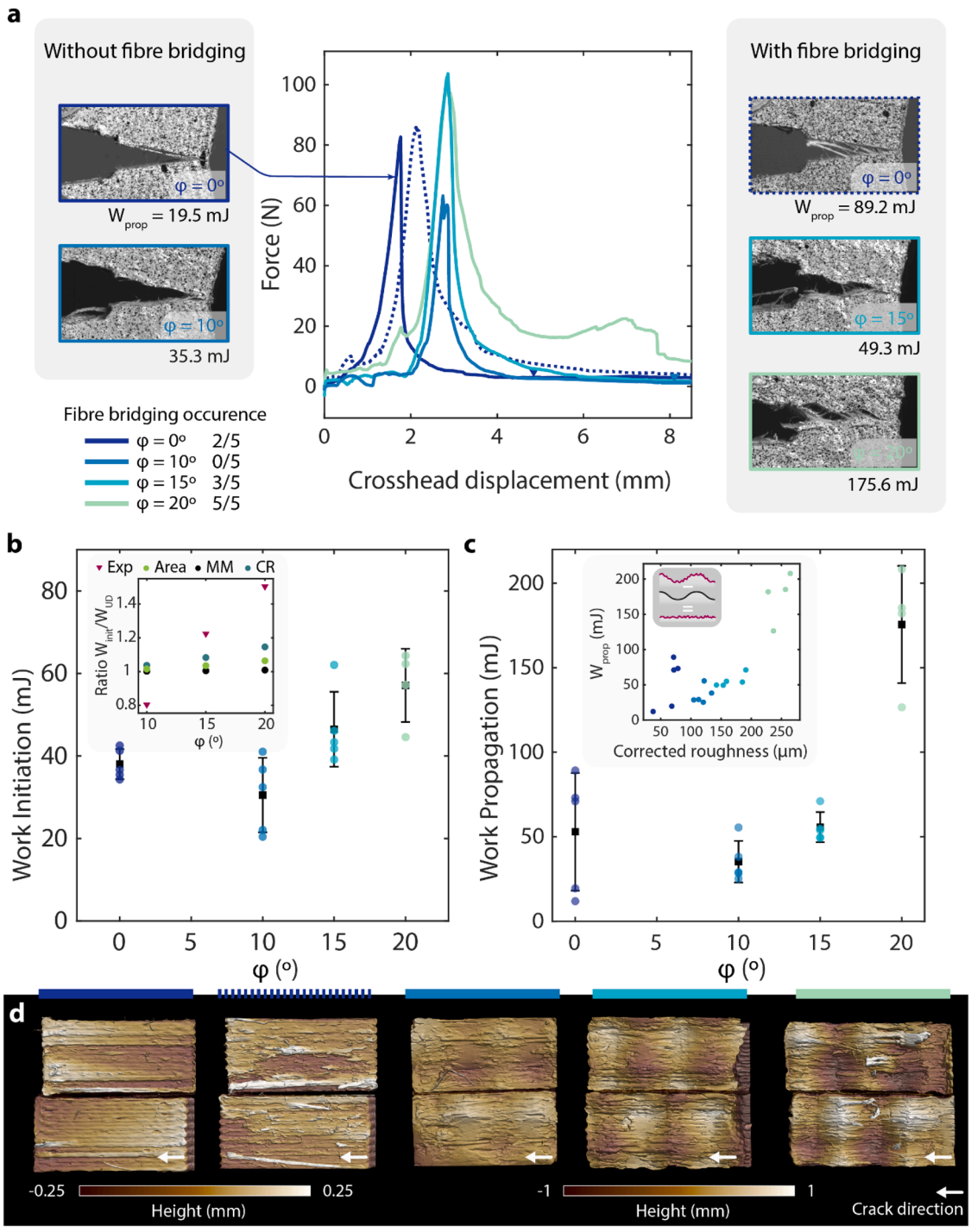

Fig. 6. Bi-sinusoidal patterns tested in Mode I loading show larger crack resistance with increasing angle. **A.** Load-displacement curves and imaging during crack-propagation of representative specimen for each configuration illustrate the area under the curve increasing with φ, and in parallel the increasing occurrence of observation of fibres bridging the crack during failure. **B.** Work exerted before max load for crack initiation indicates an initial dip in performance with $\varphi = 10°$, followed by an increase of up to 50 % for $\varphi = 20°$ as shown in the insert. The experimental *(*legend entry: *exp)* ratio W_{init}/W_{flat} is larger than what is expected from the theoretical increase in area *(Area)*, or crack resistance from Mixed-Mode *(MM^2)*, and Cotterell-Rice *(CR^2)* equations for linear elastic solids. **C.** Work after max load, corresponding to the crack propagation phase, also increases with φ. Insert shows the same data plotted against fracture surface roughness. The surface roughness is corrected to account only for local texture without the height variations linked to geometry itself. This surface roughness is obtained from **D.** height maps of the entire fracture surface, here shown for the samples pictured in **A**, also illustrating the increase in roughness with φ.

trend is as expected: the larger the amplitude and the smaller the wavelength, the poorer the performance in tension. Further, the highest stiffness and strength are found in the specimen with the smallest maximum deviation to the 0° angle. For Short-Beam Shear in Fig. 2**f,** while on average the same trend can be observed, the larger scatter does not allow to draw firm conclusions. This can also be reasoned because this type of waviness pattern does not create interlocking within the shear plane, located between layers.

The impact of waviness on tensile properties is further visualized in Fig. 2**g** where the average Young's modulus is plotted against φ, and

compared to that of LCP printed in the same condition in Gantenbein et al[39], with unidirectional samples of infill angle ranging from 0° to 90°. Classical Laminate theory describes well both the unidirectional samples, and those printed with waviness when assimilating φ to a ply direction angle. The similarity between both data sets indicates that large deviations to the 0° direction in the wavy patterns make these samples as stiff as if they were unidirectional and oriented at an angle φ. Fig. 2**g** also illustrates a scale effect. The samples with A = 0.2, λ = 2 mm and A = 0.4, λ = 4 mm both share the value $\varphi = 32.14°$ yet behave differently. The type with the smallest pattern size outperforms the larger by 33.7 %, 16.7 % and 37.6 % in SBS, Young's modulus and UTS respectively. This may be explained by more numerous interlocking zones for the smallest wavelength which provide a more homogenised stress field. This indicates that both the maximum deviation to the 0° angle and the size of a pattern seem to play a role in the stiffness and strength of parts along the longitudinal direction.

Fracture behaviour can give more insight into the performance of wavy patterns in tension with Digital Image Correlation (DIC). In Figs. 2**h**, 3D strain fields have been overlaid on photographs of tensile samples before failure. The distribution of the amplitude of the first principal strain (ϵ_1) shows that in all cases, the most strained zones are those where the maximum deviation to the 0° angle (largest slope) is located. This confirms the importance of φ, as already suggested in Fig. 2**g.** Furthermore, another effect explaining the drop in tensile performance with larger amplitudes is revealed with DIC. When the amplitude is large, the effective section width w appears to be $(w - 2A)$, as a width of A is barely strained on either side of the specimen. For instance, for A = 0.6 mm, $\epsilon_1 = 0.15$ % whereas $\epsilon_1 = 2$ % in the central areas. This corresponds to an effective width reduction of 24 %.

Overall, these elements indicate that increasing angular deviation is detrimental for both tensile and shear properties, with a larger impact on stiffness. The samples behave as weak as their weakest link when their waviness is within the loading plane.

3.2. Waviness perpendicular to the build plane

In contrast to the samples shown in Fig. 2, interfaces in wood display features that are oriented perpendicular to the loading plane to create interlocking. As a result, samples with sinusoidal variations along the XZ direction, shown in Fig. 3**a,** were also printed. Fig. 3**b** presents the parameter values chosen, and height distribution for these samples. The sample surface is also coloured according to the deviation to its average height ± 100 μm to visualize the pattern size. In Fig. 3**c**, the experimental test results are shown for UTS and short-beam shear strength. In contrast to Fig. 2**f**, increasing the maximum angle deviation φ, which is achieved here by reducing the wavelength, seems to improve short-beam shear strength for samples with waviness perpendicular to the loading direction. This may also be influenced by the finer scale of the pattern, associated with a larger density of interlocking zones.

Unlike in-plane waviness, out-of-plane waviness triggers a clear trade-off situation between tensile properties and short-beam shear strength. Increasing the wavelength increases the tensile properties as shown in Fig. 2**d and e**, while short beam shear strength decreases. In particular, at λ = 0.5 mm, short beam shear strength is the highest of all sample types and configurations tested with values close to 20 MPa.

In terms of pure tension, however, the performance of this pattern drops to 89 Mpa, which is close to the literature value of isotropic polymers like PEEK[45,46]. In comparison, the values attained in ultimate tensile strength of unidirectional samples are 426.8 ± 35 MPa for a 0° infill and 44.1 ± 2.47 MPa for 90°[39] samples. Likewise, the lowest Young's modulus is 5.5 GPa. The Young's modulus is expected to stay within the bounds given by classical laminate theory, i.e. between 2.59 ± 0.23 GPa and 17.91 ± 1.11 GPa. As the lowest bound for stiffness and strength at 90° are around the 0° values obtained for many engineering polymers without reinforcement[47,48], focus is placed on shear and toughness properties to locally strengthen junctions.

Because the difference in properties between unidirectional and wavy lines is triggered by the motion of the 3D-printer, the waviness illustrated in Fig. 3 shows a potential for a continuous transition to be made within one single-printed toolpath between straight, strong orthotropic struts and more compliant but shear-resistant interlocking junctions. In the context of applications in complex three-dimensional loading cases such as those of junctions, this directionality effect may be homogenized by using interlocking patterns on two planes simultaneously.

3.3. Waviness in two planes

To create three-dimensional interlocking patterns with waviness, a helix toolpath is investigated in Fig. 4. This helix pattern follows the curve $A_y \sin(\frac{2\pi}{\lambda}x)$ within the XY plane and $A_z \cos(\frac{2\pi}{\lambda}x)$ within the XZ plane, where A_y and A_z are the amplitudes, as shown in Fig. 4**a**. In this case A_z is restricted to 0.045 mm, while two values of A_y and λ are taken. Fig. 4**b** shows the parameters chosen and height maps of the four resulting patterns. In Fig. 4**c**, the SBS of these helicoidal samples is plotted against their amplitude in y. To study the effect of superimposing two patterns, the helix specimen with $(A_y = 0.2, \lambda = 2)$ mm can be compared both to its projection on the XY plane and to its projection on the XZ plane (i.e. same wavelength and amplitude) shown **in** Figs. 2 and 3. The helix pattern has a 9.7 % lower SBS strength than its counterpart with the projection on the XZ plane, with waviness perpendicular to the build plane. A similar decrease in SBS of 7.9 % can also be observed with $(A_y = 0.2, \lambda = 1)$ mm compared to its projection on the XZ plane. These elements indicate a negative effect of the superimposing of two patterns. In contrast, the SBS of the helix pattern with $(A_y = 0.2, \lambda = 2)$ mm is 9.3 % larger than its projection on the XY plane, i.e. with waviness within the build plane only. This increase is linked to the interlocking of the layers allowed by the waviness in the Z-direction, perpendicular to the shear plane. It is associated with a 10 % decrease in strength in line with the trade-off between short-beam shear and tensile properties determined in Fig. 3. It should however be noted that in all these cases, the difference lies within the standard deviation.

In general, Fig. 4 shows a similar trend to Fig. 2, with smaller amplitudes and wavelengths beneficial to SBS. Similarly to the XY samples, between the two samples sharing the same value of φ, the smaller pattern size performs best in terms of short-beam shear strength. This supports our hypothesis that a smaller pattern size promotes interlocking and increases resistance to interlaminar shear.

Fig. 4**d,** showing force-displacement curves and failure type for all samples, gives further credit to this argument. Within each type, the failure mode is homogeneous and is either interlaminar shear, with successive delamination, or tensile failure on the bottom of the specimen. Both types with λ = 2 mm, which perform the lowest in SBS, show interlaminar shear fracture. In contrast, the types with λ = 1 mm fail in tension. This means that the maximum interlayer shear strength has increased to a value above the maximum tensile strength for the smaller pattern size.

A helicoidal pattern has the advantage of creating both intra- and inter-laminar interlocking in shear. However, Mode-I loading can be critical for laminar materials such as 3D-printed LCP. In such loading cases, the role of interlocking is less straightforward than in shear. As a result, its impact on Mode-I crack resistance needs to be investigated.

3.4. Interlaminar fracture resistance of bi-sinusoidal shapes

The toughness in wood relies on multiple-crack arrest mechanisms, according to a Fail-safe strategy that maximises the possibility of healing when damage occurs[24]. The crack front is known to grow along regions of transversally loaded tracheids interwoven with wood rays[24]. On top of the self-healing via resin ducts for hydrophobic and antimicrobial protection, its main features are zig-zag crack deflection which

contributes to mechanical closing when the bending moment is decreased, and fibre-bridging by the tracheids[49].

Three configurations of periodic shapes are studied, with $\lambda = 5$ mm and angles φ of 10, 15 and 20° to the X-axis as shown in Fig. 5**a.** The bi-sinusoidal shape is simplified to a sawtooth pattern to minimize the number of points describing the shape and thus enable faster head movements, especially for the Z-axis. Compact Tension specimens are printed standing as depicted in Fig. 5**b**, including supports at the notch region. The zone highlighted in turquoise displays a gradual increase in the amplitude of the periodic path printed, to ensure that throughout the height of the notched region, the maximum amplitude is attained. On the rest of the specimen, flat unidirectional layers are printed to ensure comparable properties everywhere except at the notch region.

Fig. 6**a** shows typical load-displacement curves for the four specimen types, tested in Mode I. The area under the curve before and after max peak load is used to obtain a comparative work of fracture for initiation and propagation of the crack. The fracture behaviour differs significantly between samples of different patterns, related to the occurrence of a fibre bridging phenomenon. Fibre bridging seems to be more frequent as φ increases: from no occurrence at all for the five specimens tested at $\varphi = 10°$, to all five specimens showing a larger quantity of fibres pulled out at $\varphi = 20°$, as seen in the inserts. Within the group of unidirectional samples ($\varphi = 10°$), fibre-bridging is also observed in two out of the five specimens. On the load-displacement curve, this translates into a larger area under the curve after peak load. For the exemplary samples shown in the inserts, it is measured at 89 mJ with fibre-bridging (shown by blue dashed lines), compared to 19 mJ without (blue full lines). Fibre-bridging at the scale of printed lines detaching seems to be related to an increase in area under the curve after peak load, which can be expected as this is a typical extrinsic toughening mechanism, in wood[49] and other fibrous materials[50]. However, another qualitative effect other than fibre-bridging that influences the area under the curve after peak load should also be noted. A secondary bump well after maximum peak load can be noticed at the load-displacement curve of the $\varphi = 20°$ example. This bump is present for four out of the five $\varphi = 20°$ samples. It is absent in some samples where fibre-bridging was also observed. The presence of these qualitative effects translate directly into toughness performance.

In Fig. 6**b**, work exerted for the initiation of the crack is shown for the straight and three wavy configurations. In theory, increasing φ is indeed expected to improve performance in toughness via several geometrical contributions. Three of these are considered here. First, Cotterell and Rice[51] have for instance developed a ratio of stress-intensity factors at the tip of a slightly curved crack. This ratio has been shown by Zavattieri et al[52]. to characterize well a sine crack between linear elastic solids with $A/\lambda < 0.25$. Our maximum A/λ is well below this value, with 0.091. The equation describing the ratio of the stress-intensity factor of a curved crack over the flat equivalent is:

$$CR = \frac{K_{IC}}{K_0} = \frac{2}{1 + \left[1 + 4\pi^2 \left(\frac{A}{\lambda}\right)^2\right]^{-\frac{1}{2}}}$$

This value is plotted for the different patterns in the insert of Fig. 6**b** under the legend entry *CR*. Again in the linear elastic fracture mechanics (LEFM) framework, Hutchinson and Suo[53] have calculated a similar ratio focusing on mixed mode cracking, $MM = \frac{R}{R1} = \left(1 + (\eta - 1)\sin^2\psi\right)^{-1}$ where $\eta = 0.7$ for a rather ductile material and $\psi = \tan^{-1}(K_{IIeff}/K_{Ieff})$. The ratio K_{IIeff}/K_{Ieff} is a function of φ only. Since the maximum calculated ψ in our case is 10°, this ratio stays very close to 1, as shown with the legend entry *MM* in the same graph. Finally, the increase in surface area of a sinusoidal pattern over a planar version can also be considered, with a corresponding ratio $Area = 1/\cos\varphi$. For $\varphi = 10°$, $\varphi = 15°$ and $\varphi = 20°$, this area increase is 2.0, 5.0 and 9.2 % respectively, compared to the flat zone.

These theoretical ratios are all compared in the insert of Fig. 6**b** to the experimental ratio measured between work to initiate the crack in the patterned and unidirectional surfaces. Both CR and MM are ratios of fracture toughness K_{ic}. In LEFM under plane strain, the relationship between G, the energy release rate, and K_{ic} is quadratic. In order to be comparable to the experimental ratio of work, these ratios are squared on the graph. While they are derived for LEFM which does not apply here, they can shed light on the theoretical contribution of the geometry versus that of LCP's characteristics such as its fibrillar microstructure. The general trend of experiments does show an increase in W_{init} with φ. However, the average value at $\varphi = 10°$ is smaller than the average for unidirectional samples. The value should not be below 1 in theory, and is here close to 0.8, indicating poor adhesion between layers. The total absence of fibre-bridging noticed at $\varphi = 10°$ is another symptom of lower adhesion. This may be explained by manufacturing differences, such as the influence of speed: it is indeed much slower to print one layer with waviness, which may decrease interlayer adhesion as the time elapsed between the deposition of two neighbouring lines, and layers, is larger. Due to the large movements in the Z-direction, which is a slower, threaded axis on our 3D printer, the printing duration is 34 s for one flat layer, and 64.5, 68.9, and 75.6 s respectively for one layer at $\varphi = 10°$, $\varphi = 15°$ and $\varphi = 20°$. It is possible that the smaller interlocking seen at $\varphi = 10°$ does not counterbalance the change in manufacturing conditions such as lower speeds. A systematic study on the influence of speed on the adhesion of LCP should therefore be carried out in future work.

Furthermore, the increase in W_{init} with $\varphi = 15°$ and $\varphi = 20°$ over unidirectional samples is noticeable. If the three theoretical contributions are combined (CR^2: increase due to crack tip deviation, MM^2 mixed mode loading, and *Area* as crack surface increases), a 42 % increase is expected for $\varphi = 20°$, when the experimental improvement is closer to 50 %. For $\varphi = 15°$, the theoretical ratio of 1.227 matches with the experimental value of 1.222.

A similar trend as that seen for W_{init} is noticed for W_{prop}, the work measured after maximum load, which is related to the propagation of the crack. It is in fact even more marked, as shown in Fig. 6**c**. The increase with φ is in this case up to three-fold larger than that of the average unidirectional specimen for $\varphi = 20°$. Another more pronounced trend is the lower performance of W_{prop} for $\varphi = 10°$ compared to the unidirectional samples, with $\frac{W_{\text{prop},\varphi=10°}}{W_{\text{prop,flat}}} = 0.66$ compared to the previous ratio $\frac{W_{\text{init},\varphi=10°}}{W_{\text{init,flat}}} = 0.80$. Again, this could be attributed to lower adhesion combined with a lack of interlocking for this sample geometry. As an indication of the importance of fibre bridging, a distinction of the performance of specimens with and without its occurrence can be made using unidirectional specimens. Three specimens which display fibre bridging have an average W_{prop} of 78 mJ. The other two which do not show bridging have an average W_{prop} of 16 mJ. The average increase with $\varphi = 10°$ is 76 % compared to the lower baseline value for flat samples without fibre bridging. However, the occurrence of fibre bridging in flat samples may be stochastic as it is not triggered by printing parameters. Therefore, for all other purposes, comparisons should use the total range of samples, with and without bridging.

To further investigate the toughening role of the different patterns, fracture surface roughness is measured on fractured surfaces. It is plotted as an insert in Fig. 6**c** against W_{prop}. One may first observe that roughness seems consistent within each specimen type and an average increase with φ is noticed. Moreover, specimens with the largest surface roughness seem to also display the largest W_{prop}. Surface roughness quantifies distributed damage such as the pull-out of short fibrils, and even cohesive fracture zones within a layer, whose areas are seen to increase with φ in Fig. 6**d.** However, local damage due to individual, macroscopic fibre bridging is less readily captured with surface roughness. Again, this can be observed with the two distinct unidirectional sample behaviours, with and without fibre-bridging. The two leftmost height maps of Fig. 6**d** show the exemplary unidirectional sample

displaying fibre-bridging and another one without. The surface roughness (Sa) of the sample displaying fibre-bridging is 71.4, compared to 68.4 for the specimen for which the crack has propagated between two layers, but without any pulled-out fibre observed. Sa quantifies the average difference in height of each point compared to the arithmetical mean of the idealized smooth surface. A single fibre bridging the crack and pulling out until total fracture may contribute significantly to enhance W_{prop} but will not be captured with Sa, illustrating the limits of fracture surface roughness as a metric to quantify this phenomenon. On the fracture surfaces, one may also note that the smoother areas tend to be those located at the crests and troughs of the bi-sinusoidal shape. These smooth regions represent a large proportion of the total area for $\varphi = 10°$. They decrease in size for $\varphi = 15°$ and are non-existent for $\varphi = 20°$. Instead of smooth surfaces, one can distinguish between individual torn printed paths. In **Figure SI 1**, the fracture surface areas of three samples are observed with scanning electron microscopy (SEM). The two flat samples, with and without macro-scale fibre bridging, display relatively little plasticity at micro-scale, in contrast to the the sample with $\varphi = 20°$, showing a rougher fracture surface with many pulled out fibres and fibrils. This may indicate that the relatively higher shear forces favoured by a steeper φ are very effective at provoking plastic deformation such as local fibril pull-out, and larger fibre bridging. Being loaded in tension, they can simultaneously shield the crack and also dissipate energy in LCP better than what may theoretically expected from geometrical arguments and LEFM.

In summary, these elements suggest that the combination of bridging and deviation are the main mechanisms responsible for the increasing fracture energy with increasing φ. At most, increasing crack area of 9.2 % with the largest φ may play a role, but cannot explain the average increase in work after fracture from 53 mJ to 176 mJ, i.e. more than three-fold increase from the straight specimen. This improvement may be attributed to the more tortuous crack geometry and the plasticity induced by the increased mode-mixity effect in LCP. We hypothesize that the shear stresses introduced at the steepest locations of the bi-

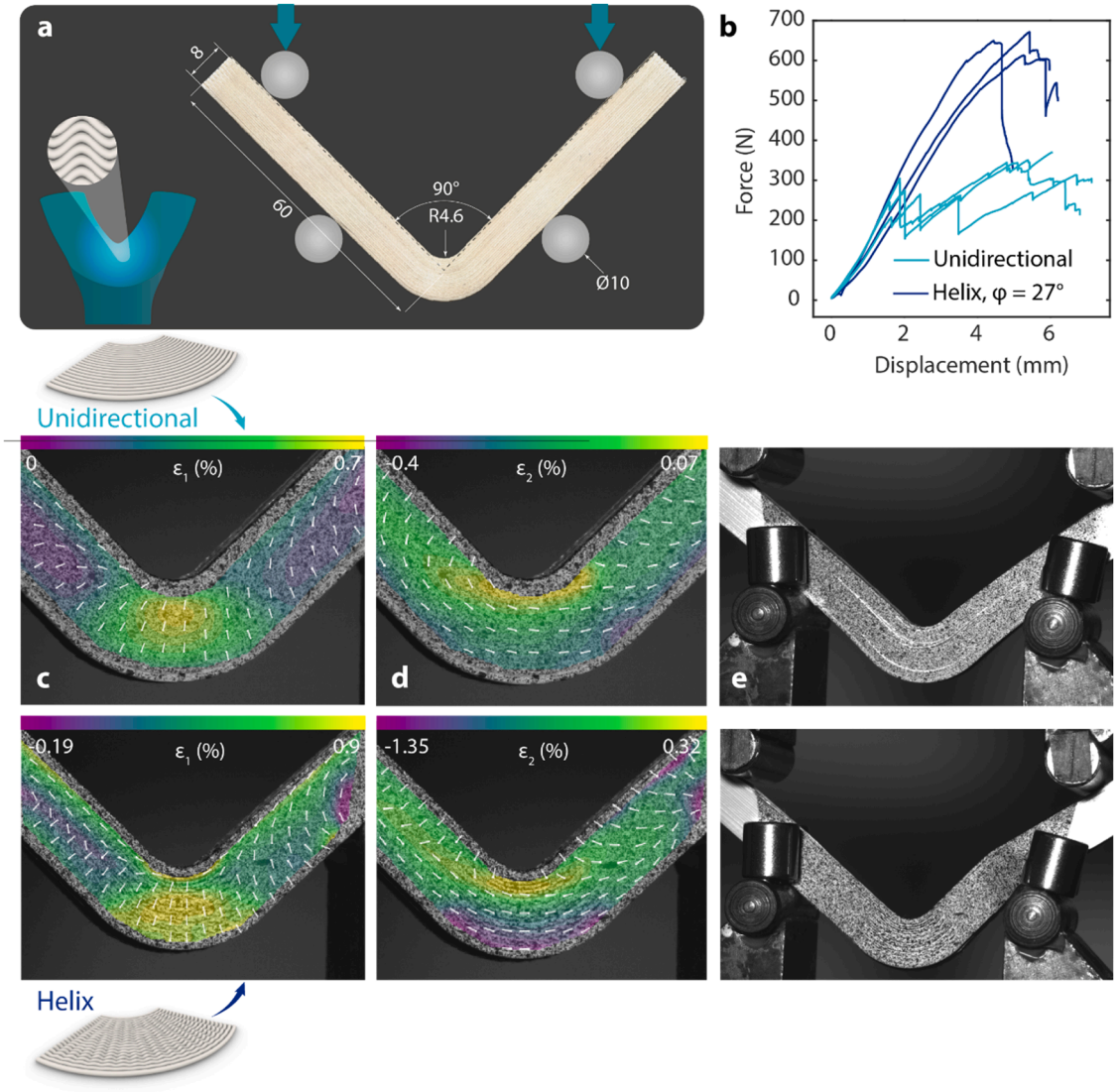

Fig. 7. Four-point bending of an elbow-like junction compares the behaviour of a contour-like pattern to a helical pattern. **A.** Dimensions of the curved beam and test set-up. The thickness of the beam is 10 mm **B.** Force-displacement curves show that the unidirectional samples reach about half the load of the Helix samples. Digital Image correlation of unidirectional (top) and Helix (bottom) samples gives further insight into their fracture mechanisms. Colours and arrow orientation represent respectively the amplitude and direction of the principal strain ϵ_1 in **C** and the second principal strain ϵ_2 in **D.** Photographs of the same specimen after final fracture illustrate the two different behaviours in **E.** The unidirectional specimens all delaminate early, and continue deforming with successive propagation or opening of delamination. In contrast, the helix specimens show close to a three-times larger strain before the first failure. Furthermore, failure also does not occur at the junction zone but in the indentation point of a strut, indicating superior resistance of the Helix zone compared to unidirectional samples.

sinusoidal shapes become large enough at $\varphi = 15°$ and $\varphi = 20°$ to provoke a widespread pull-out of the fibrils involved at the interface, thereby promoting a more tortuous crack growth and increased energy dissipation, in a similar fashion to wood fracture.

In future designs, the study of crack propagation should include high-resolution imaging to quantify the influence of micro- and macroscopic fibre bridging. It should also relate to recent modelling efforts, especially using cohesive fracture models similar to those developed for wood[49]. Moreover, because of the similarities with wood, in particular the highly fibrillar structure of this anisotropic material, it could also be used to replicate and study such bio-materials, which are often influenced during lifespan by external factors.

3.5. Junctions with helix patterns

Mode-I toughness is an important component in increasing the robustness of materials, however, the loading configuration of a junction is often more complex. To represent a junction, the geometry shown in Fig. 7**a** is chosen for its ability to produce a tensile stress normal to the fibre direction in a confined zone. The geometry replicates a two-strut junction, or a three-strut junction without external loading on the last strut, subjected to a worse-case loading scenario. The stress state of such a shape in four-point bending consists of the following components: Circumferential tensile stresses along the inner surface, circumferential compressive stresses along the outer surface, radial tensile stresses, from 0 at the inner and outermost surfaces with a peak in the middle third of the thickness[54,55]. The potential reinforcing effect of waviness is assessed with a helix toolpath shown enlarged in **Figure SI 2a** and compared to a unidirectional pattern, in which print paths follow the contour of the curved beam. The helix pattern is only applied to the curved zone, while the struts are printed unidirectional for both types to provide consistent strut arm stiffness between the two sample types. The parameters of the helix are chosen to summarize previous learnings. A pattern size with a wavelength of 1 mm is chosen, according to Fig. 4. The amplitude A should be as high as possible considering that Fig. 6 indicates that toughness is improved with increasing φ. However, manufacturing-wise, a too large amplitude shows risk of collision with the print bed on the first layer, and the nozzle tip also risks ploughing into deposited materials. Therefore, a sinusoidal amplitude A of 80 % of a printed layer of 0.1 mm is chosen. This leads to a value of $\varphi_{max} = 27°$. This value corresponds to a sinusoidal amplitude of 80 % of a printed layer of 0.1 mm. Height maps of the printed unidirectional and helix junctions are shown in **Figure SI 2b**.

The load displacement curve of the specimen subjected to four-point bending are shown in Fig. 7**b**. A clear distinction in overall performance and fracture behaviour can be made between the unidirectional and the helix samples. With 645 ± 29 N, the helix samples attain a max load on average 88 % larger than the unidirectional samples (342 ± 28 N). The strain attained at max failure is also 2.96 times larger for the helix samples, without any significant increase in mass, as shown in **Table SI 1.** In Fig. 7**c,** the amplitude and direction of first principal strain ϵ_1 obtained by DIC are overlaid onto the two configurations just before the onset of their first load drop. In both cases, ϵ_1 in the curved zone is a tensile radial strain as indicated by the arrows and positive value. However, the distribution of maximum amplitude is more concentrated on the unidirectional specimen than on the helix one. This zone is the one where the first delamination takes place in the unidirectional pattern, corresponding to the middle third of the sample width as expected. In contrast, for the helix specimen the maximum ϵ_1 is seen on the entire patterned zone, indicating a more even distribution of strain which contributes to delay the onset of fracture. The second principal stresses are shown in Fig. 7**d**, with the expected tensile and compressive circumferential stresses.

Both configurations before test arrest, which is set to not exceed 7 mm of cross-head displacement, are illustrated in Fig. 7**e.** The fracture behaviour differs between the two types. The unidirectional samples crack earlier but can carry a load close to P_{max} via the continued onset and propagation of delamination until the test is interrupted. In contrast, the helix samples break catastrophically at P_{max} via strut failure at a contact point to the fixture. As a result, the junction zone was not tested to its fullest potential and may be capable of carrying even more load in this configuration if the struts are stiffened by doublers. Since the struts are the same unidirectional LCP in both types, these elements indicate that wherever the unidirectional configuration is prone to early failure because of radial tensile loading, the helix pattern can indeed be implemented to impart robustness.

To illustrate the potential of this method at reinforcing junctions in TAO parts, a sinusoidal pattern is applied for illustration purposes to a three-strut junction in Fig. 8. In a TAO part such as the one printed with LCP in Fig. 8**a**, an optimal load transfer can be ensured by continuous printed lines across the different struts. Such a part possesses many kinds of junction configurations, including two- and three-strut junctions. Three two-strut junctions similar to those tested in Fig. 7 can be rotated and adapted to create a three-strut junction, as shown in Figs. 8**b and** 8**c**. The 3D-printed junction with interlocked continuous toolpaths between all struts is shown in Fig. 8**d**.

4. Conclusions

For a 2D sinewave pattern lying within the building plane, larger amplitude and smaller wavelength are detrimental to performance in tension. The maximum angle of deviation between the sinewave and the X-axis, named φ, is shown to play an important role. In general, the samples behave as stiff as if they were unidirectional but oriented at the angle φ, following the corresponding expected behaviour from Classical Laminate theory. For a sinusoidal pattern lying perpendicular to the build plane (leading to non-planar layers) while a similar trend can be noticed in tension, short-beam shear performance increases due to layer interlocking.

Bi-sinusoidal patterns studied in Mode-I fracture resistance with the largest φ show a 50 % increase in work exerted before peak load, and a three-fold increase in work exerted for crack propagation. An increase of the surface roughness and macroscopic fibre-bridging is observed with increasing φ. These elements may indicate that the rising ratio of Mode-II loading introduced with larger φ leads to enough shear stresses being applied to the interface to pull out the fibrillar microstructure, thus dissipating more energy and slowing the crack propagation, similar to

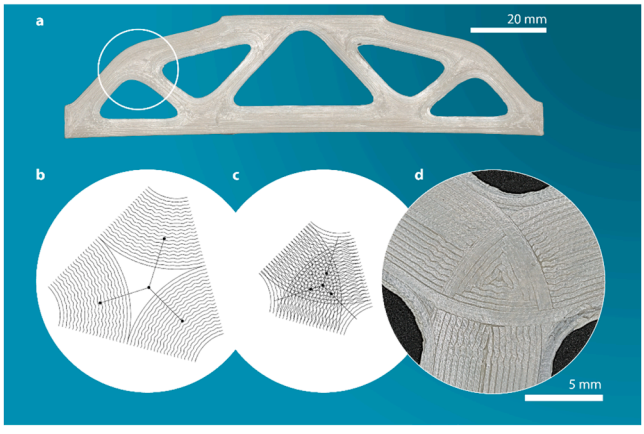

Fig. 8. The sinusoidal pattern can also be applied on a three-strut junction. **A.** A typical bridge-like topology optimized part contains sets of two-strut, three-strut and four-strut junctions. This part is printed with LCP using a fully dense concentric infill without waviness. **B.** A three-strut junction can be made of three sets of continuous paths with waviness, each of them being a two-strut junction. **C.** These paths can be overlapped, and **D.** 3D-printed, creating interlocking within the junction while remaining continuous to transfer the loads from one strut to the next.

fibres in wood.

To test a junction zone, a helical pattern of a curved beam was loaded under four-point bending. Compared to the same geometry without the pattern, the failure load is improved by 88 % without additional mass. Strain-to-failure is also close to three-fold larger since the unidirectional specimens delaminate when exposed to radial tensile stresses. Combined with the development of new topology optimisation schemes, this approach opens avenues for higher structural performance with only marginal extra energy or material consumption. By utilizing the synergy between anisotropic materials and geometric patterns, designers can blend material properties to tune compliance, strengthen weak regions or redistribute loads, with the frugality and elegance of natural materials produced by living organisms.

CRediT authorship contribution statement

Caroline Houriet: Writing – review & editing, Writing – original draft, Visualization, Investigation, Formal analysis, Conceptualization. **Boris Ulyanov:** Writing – review & editing, Formal analysis. **John-Alan Pascoe:** Writing – review & editing, Investigation. **Kunal Masania:** Writing – review & editing, Writing – original draft, Visualization, Supervision, Resources, Investigation, Funding acquisition, Formal analysis, Conceptualization.

Declaration of Competing Interest

K.M. is co-founder of NematX AG which develops 3D-printed high performance polymers.

Acknowledgements

K.M. and C.H. acknowledge the support of ESA co-sponsored Research grant No. 4000131850.

Author agreement statement

We the undersigned declare that this manuscript is original, has not been published before and is not currently being considered for publication elsewhere.

We confirm that the manuscript has been read and approved by all named authors and that there are no other persons who satisfied the criteria for authorship but are not listed. We further confirm that the order of authors listed in the manuscript has been approved by all of us.

We understand that the Corresponding Author is the sole contact for the Editorial process. He/she is responsible for communicating with the other authors about progress, submissions of revisions and final approval of proofs Signed by all authors as follows:

Appendix A. Supporting information

Supplementary data associated with this article can be found in the online version at doi:10.1016/j.addma.2024.104590.

Data availability

Data will be made available on request.

References

[1] R. Weinkamer, P. Fratzl, Mater. Sci. Eng. C. 31 (2011) 1164.
[2] M.P. Schmidt, L. Couret, C. Gout, C.B.W. Pedersen, Struct. Multidiscip. Optim. 62 (2020) 3105.
[3] D.R. Jantos, K. Hackl, P. Junker, Struct. Multidiscip. Optim. 61 (2020) 2135.
[4] L. Vertonghen, F.X. Irisarri, D. Bettebghor, B. Desmorat, Comput. Methods Appl. Mech. Eng. 412 (2023) 116069.
[5] R.D. Kundu, X.S. Zhang, Compos. Struct. 320 (2023) 117041.
[6] N.S. Hmeidat, B. Brown, X. Jia, N. Vermaak, B. Compton, Rapid Prototyp. J. 27 (2021) 1467.
[7] N. Ranaivomiarana, D. Bettebghor, B. Desmorat, Adv. Struct. Multidiscip. Optim. (2018), https://doi.org/10.1007/978-3-319-67988-4.
[8] R.D. Kundu, X.S. Zhang, Addit. Manuf. 75 (2023) 103730.
[9] S. Kumar, S. Tan, L. Zheng, D.M. Kochmann, npj Comput. Mater. 6 (2020) 1.
[10] Z. Wang, R. Dabaja, L. Chen, M. Banu, Sci. Rep. 13 (2023) 1.
[11] A. Di Rienzo, E. Duriez, M. Charlotte, J. Morlier, Mech. Ind. 25 (2024), https://doi.org/10.1051/meca/2024004.
[12] J.R. Raney, B.G. Compton, J. Mueller, T.J. Ober, K. Shea, J.A. Lewis, Proc. Natl. Acad. Sci. U. S. A. 115 (2018) 1198.
[13] P.A.G.S. Giachini, S.S. Gupta, W. Wang, D. Wood, M. Yunusa, E. Baharlou, M. Sitti, A. Menges, Sci. Adv. 6 (2020) 1.
[14] D. Kokkinis, F. Bouville, A.R. Studart, Adv. Mater. 30 (2018) 1.
[15] N.M. Larson, J. Mueller, A. Chortos, Z.S. Davidson, D.R. Clarke, J.A. Lewis, Nature 613 (2023) 682.
[16] L. Ren, Z. Wang, L. Ren, Z. Han, Q. Liu, Z. Song, Compos. Part B Eng. 242 (2022) 110086.
[17] D. Christophe, R. David, S. Duncan, J. Bot. Res. 3 (2020) 100.
[18] D. Slater, R. Ennos, Arboric. J. 37 (2015) 21.
[19] D. Slater, R.S. Bradley, P.J. Withers, A.Roland Ennos, Trees - Struct. Funct. 28 (2014) 1437.
[20] M.J. Jaffe, S. Forbes, Plant Growth Regul. 12 (1993) 313.
[21] D. Slater, Trees 35 (2021) 513.
[22] S. Özden, D. Slater, R. Ennos, Trees - Struct. Funct. 31 (2017) 903.
[23] M.C. Maaß, S. Saleh, H. Militz, C.A. Volkert, Adv. Mater. 32 (2020), https://doi.org/10.1002/adma.201907693.
[24] U. Müller, W. Gindl-Altmutter, J. Konnerth, G.A. Maier, J. Keckes, Sci. Rep. 5 (2015) 1.
[25] H.L. Duhamel du Monceau, *De l'exploitation Des Bois: Seconde Partie*, Paris, 1764.
[26] X. Wang, W. Gard, H. Borska, B. Ursem, J.W. van de Kuilen, Eur. J. Wood. Wood. Prod. (2020) 102.
[27] Z. Liu, Z. Zhang, R.O. Ritchie, Acta Biomater. 102 (2020) 75.
[28] J. Allum, J. Kitzinger, Y. Li, V.V. Silberschmidt, A. Gleadall, Addit. Manuf. 38 (2021) 101715.
[29] Z. Jia, L. Wang, Acta Mater. 173 (2019) 61.
[30] I.A. Malik, M. Mirkhalaf, F. Barthelat, J. Mech. Phys. Solids 102 (2017) 224.
[31] L. Mencattelli, S.T. Pinho, Compos. Sci. Technol. 190 (2020) 108047.
[32] V. Damodaran, A.G. Castellanos, M. Milostan, P. Prabhakar, Mater. Des. 157 (2018) 60.
[33] M. Zhang, J. Zhang, D. Yang, Y. Li, X. Cui, K. Fu, Addit. Manuf. 79 (2024) 103936.
[34] A. Selvam, S. Mayilswamy, R. Whenish, J. Vinyl Addit. Technol. 26 (2020) 511.
[35] L.A. Burns, A.P. Mouritz, D. Pook, S. Feih, Compos. Struct. 94 (2012) 995.
[36] L. Zorzetto, D. Ruffoni, Adv. Funct. Mater. 29 (2019) 1.
[37] H. Liu, X. Wang, L. Wan, J. Hao, Y. Zhong, Z. Mao, H. Wang, Z. Cao, S. Wang, J. Lu, J. Mech. Phys. Solids 188 (2024) 105679.
[38] C. Houriet, V. Damodaran, C. Mascolo, S. Gantenbein, D. Peeters, K. Masania, Adv. Mater. 2307444 (2023) 1.
[39] S. Gantenbein, K. Masania, W. Woigk, J.P.W. Sesseg, T.A. Tervoort, A.R. Studart, Nature 561 (2018) 226.
[40] S.D. Hudson, A.J. Lovinger, Polym. (Guildf.) 34 (1993) 1123.
[41] Y. Ide, Z. Ophir, Polym. Eng. Sci. 23 (1983) 261.
[42] C. Houriet, E. Claassen, C. Mascolo, H. Jöhri, A. Brieva, S. Szmolka, S. Vincent-Bonnieu, R. Heeb, S. Gantenbein, U. Lafont, T. Rohr, K. Masania, Adv. Mater. Technol. (2024), https://doi.org/10.1002/admt.202400571.
[43] S. Gantenbein, C. Mascolo, C. Houriet, R. Zboray, A. Neels, K. Masania, A. R. Studart, Adv. Funct. Mater. (2021) 2104574.
[44] R. Schaller, T. Peijs, T.A. Tervoort, Compos. Part A Appl. Sci. Manuf. 81 (2016) 296.
[45] I. Vindokurov, Y. Pirogova, M. Tashkinov, V.V. Silberschmidt, Polym. (Basel) 14 (2022) 0.
[46] Q. Xu, W. Xu, Y. Yang, X. Yin, C. Zhou, J. Han, X. Li, Y. Shang, H. Zhang, Addit. Manuf. 55 (2022), https://doi.org/10.1016/j.addma.2022.102852.
[47] G. Zhang, Q. Wang, Y. Ni, P. Liu, F. Liu, D. Leguillon, L.R. Xu, Polym. Test. 117 (2023) 107845.
[48] J.W. Nelson, D. Atkins, M.L. Gottstine, J. Yang, G. Garapic, S. Jaminion, A. Nelson, K. Wilson, Rapid Prototyp. J. 26 (2020) 1453.
[49] B. Mirzaei, A. Sinha, J.A. Nairn, Compos. Sci. Technol. 128 (2016) 65.
[50] R. Khan, Compos. Struct. 229 (2019), https://doi.org/10.1016/j.compstruct.2019.111418.
[51] B. Cotterell, J.R. Rice, Int. J. Fract. 16 (1980) 155.
[52] P.D. Zavattieri, L.G. Hector, A.F. Bower, Int. J. Fract. 145 (2007) 167.
[53] J.W. Hutchinson, Z. Suo, Mixed Mode Crack. Layer. Mater. (1976).
[54] G. Kress, R. Roos, M. Barbezat, C. Dransfeld, P. Ermanni, Compos. Struct. 69 (2005) 458.
[55] S. Süsler, Z. Kazancı, Polym. (Basel) 15 (2023), https://doi.org/10.3390/polym15193928.